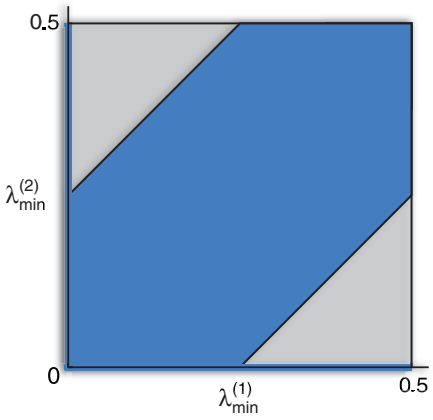

Fig. 3. Witnessing genuine multipartite entanglement. The figure displays the 2D cross section through the six-qubit eigenvalue polytope where we fix $\lambda^{(3)}_{min} = \ldots = \lambda^{(6)}_{min} = 0.125$. If the local eigenvalues do not belong to any of the biseparable entanglement polytopes (blue region), then all corresponding pure states necessarily contain genuine six-qubit entanglement.

the global state to estimate the purity (*22*). Whereas it is an experimental challenge to achieve the levels of purity necessary for the application of our method, we believe that they are in the reach of current technology (*23*–*25*).

References and Notes

1. G. Vidal, *Phys. Rev. Lett.* **91**, 147902 (2003).
2. D. Leibfried *et al*., *Science* **304**, 1476 (2004).
3. V. Giovannetti, S. Lloyd, L. Maccone, *Science* **306**, 1330 (2004).
4. R. Horodecki, P. Horodecki, M. Horodecki, K. Horodecki, *Rev. Mod. Phys.* **81**, 865 (2009).
5. C. H. Bennett, S. Popescu, D. Rohrlich, J. A. Smolin, A. V. Thapliyal, *Phys. Rev. A* **63**, 012307 (2000).
6. W. Dür, G. Vidal, J. I. Cirac, *Phys. Rev. A* **62**, 062314 (2000).
7. D. M. Greenberger, M. A. Horne, A. Zeilinger, in *Bell's Theorem, Quantum Theory, and Conceptions of the Universe*, M. Kafatos, Ed. (Kluwer, 1989), pp. 69–72.
8. F. Verstraete, J. Dehaene, B. De Moor, H. Verschelde, *Phys. Rev. A* **65**, 052112 (2002).
9. M. Christandl, G. Mitchison, *Commun. Math. Phys.* **261**, 789 (2006).
10. A. Klyachko, Quantum marginal problem and representations of the symmetric group, arXiv:quant-ph/0409113 (2004).
11. S. Daftuar, P. Hayden, *Ann. Phys.* **315**, 80 (2005).
12. A. J. Coleman, V. I. Yukalov, *Reduced Density Matrices: Coulson's Challenge* (Springer, 2000).
13. A. Klyachko, *J. Phys. Conf. Ser.* **36**, 72 (2006).
14. Further details can be found in the supplementary text on *Science* Online.
15. M. Brion, in *Séminaire d'Algèbre P. Dubreil et M.-P. Malliavin*, M. P. Malliavin, Ed. (Springer, 1987), pp. 177–192.
16. H. Derksen, G. Kemper, *Computational Invariant Theory* (Springer, 2002).
17. B. Doran, F. Kirwan, *Pure Appl. Math. Q.* **3**, 61 (2007).
18. Y.-J. Han, Y.-S. Zhang, G.-C. Guo, *Phys. Rev. A* **70**, 042309 (2004).
19. O. Gühne, G. Toth, H. J. Briegel, *New J. Phys.* **7**, 229 (2005).
20. R. E. Borland, K. Dennis, *J. Phys. B* **5**, 7 (1972).
21. K. Furuya, M. C. Nemes, G. Q. Pellegrino, *Phys. Rev. Lett.* **80**, 5524 (1998).
22. H. Buhrman, R. Cleve, J. Watrous, R. de Wolf, *Phys. Rev. Lett.* **87**, 167902 (2001).
23. A. Rauschenbeutel *et al*., *Science* **288**, 2024 (2000).
24. J.-W. Pan, M. Daniell, S. Gasparoni, G. Weihs, A. Zeilinger, *Phys. Rev. Lett.* **86**, 4435 (2001).
25. T. Monz *et al*., *Phys. Rev. Lett.* **106**, 130506 (2011).
26. M. Walter, B. Doran, D. Gross, M. Christandl, www.entanglement-polytopes.org (2012).

Acknowledgments: We thank A. Botero, F. Brandão, P. Bürgisser, C. Ikenmeyer, F. Kirwan, F. Mintert, G. Mitchison, A. Osterloh, and P. Vrana for valuable discussions. This work is supported by the German Science Foundation (grant CH 843/2-1), the Swiss National Science Foundation [grants PP00P2_128455, 20CH21_138799 (CHIST-ERA project CQC), and 200021_138071], the Swiss National Center of Competence in Research Quantum Science and Technology, and the Excellence Initiative of the German Federal and State Governments (grant ZUK 43). After completion of this work, we have learned about independent related work by Sawicki, Oszmaniec, and Kuś.

Supplementary Materials

www.sciencemag.org/cgi/content/full/340/6137/1205/DC1
Supplementary Text
Figs. S1 to S4
Tables S1 to S3
References (*27*–*82*)

19 November 2012; accepted 25 April 2013
10.1126/science.1232957

From Sub-Rayleigh to Supershear Ruptures During Stick-Slip Experiments on Crustal Rocks

François X. Passelègue,[1]* Alexandre Schubnel,[1] Stefan Nielsen,[2] Harsha S. Bhat,[3] Raùl Madariaga[1]

Supershear earthquake ruptures propagate faster than the shear wave velocity. Although there is evidence that this occurs in nature, it has not been experimentally demonstrated with the use of crustal rocks. We performed stick-slip experiments with Westerly granite under controlled upper-crustal stress conditions. Supershear ruptures systematically occur when the normal stress exceeds 43 megapascals (MPa) with resulting stress drops on the order of 3 to 25 MPa, comparable to the stress drops inferred by seismology for crustal earthquakes. In our experiments, the sub-Rayleigh–to–supershear transition length is a few centimeters at most, suggesting that the rupture of asperities along a fault may propagate locally at supershear velocities. In turn, these sudden accelerations and decelerations could play an important role in the generation of high-frequency radiation and the overall rupture-energy budget.

Earthquake damage depends, in part, on the velocity of the rupture front (*1*). In 1973, Burridge demonstrated theoretically that in-plane shear ruptures (mode II) could propagate at velocities higher than the shear wave velocity (C_s) and up to the compressional wave velocity (C_p) (*2*). Since then, so-called supershear ruptures ($V_r > C_s$, where V_r is rupture velocity) have been observed during large strike-slip earthquakes (*3*–*8*). The stress and geometric conditions leading to the transition between sub-Rayleigh and supershear ruptures have been investigated with photoelasticity, both theoretically (*9*, *10*) and experimentally, on brittle polymers (*11*–*15*). Although these experiments successfully illustrate supershear ruptures, the lack of experiments on rock samples limits the ability to understand these rare events observed in nature. In a recent experimental study, a photoelastic setup was coupled with an acoustic high-frequency–recording multistation array during stick-slip experiments on polycarbonate sheets. This allowed Schubnel *et al*. to use high-frequency acoustics to identify unequivocally the signature of both sub-Rayleigh and supershear ruptures (*15*). This advance has opened the possibility of revisiting experimental work performed on rocks (*16*–*19*).

Here, we report results from stick-slip experiments conducted on saw-cut Westerly granite samples (fig. S1), which serve as proxies for crustal rocks, during triaxial loading (where the

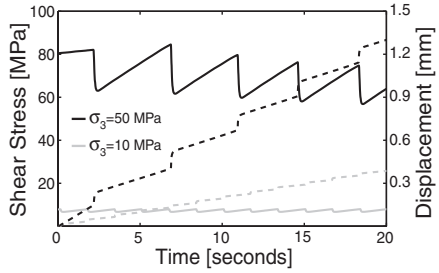

Fig. 1. Stress release during microearthquakes. Evolution of shear stress (solid lines) and displacement (dashed lines) is represented for two stick-slip experiments conducted at 10- and 50-MPa confining pressure.

[1]Laboratoire de Géologie, CNRS UMR 8538, École Normale Supérieure, 75005 Paris, France. [2]Istituto Nazionale di Geofisica e Vulcanologia, Roma 00143, Italy. [3]Institut de Physique du Globe de Paris, 1 rue Jussieu, 75238 cedex 05 Paris, France.

*Corresponding author. E-mail: passelegue@geologie.ens.fr

principal stresses $\sigma_1 > \sigma_2 = \sigma_3$). Stick-slip experiments and earthquake mechanisms are analogous in nature because they both result from rapid frictional sliding along preexisting faults, leading to partial or total stress drop (*16*). In our experiments, the stress conditions were typical of the upper crust, ranging from 10 to 150 MPa in normal stress acting on the preexisting fault. In total, we recorded more than 200 stick-slip events (Fig. 1). For each event, we inverted the rupture velocity directly from our experimental records, using high-frequency acoustics as a tracking tool (fig. S2).

We used recorded accelerograms to track the Mach wavefront arrival. Theoretical arrival time of the Mach wavefront radiated away from the rupture tip was predicted using (i) the position of the rupture front determined from the inverted rupture velocity (fig. S2) and (ii) the shear wave velocity and the distance between the Mach front antenna (MFA) sensors to the fault, as defined in Fig. 2A (*15*). Our calculation assumes that the rupture velocity is constant. Importantly, we looked for ruptures with V_r greater than the shear wave speed but different that $\sqrt{2}C_s$, for in this case, no Mach cone is expected (*20*).

We compared our calculation with waveforms recorded by the MFA array for a stick-slip event during which a supershear rupture velocity was predicted by the inversion (Fig. 2B). In agreement with theory (*21*), we first observed a weak *P*-wave arrival, which corresponds to the continuous emission of *P* waves by the rupture tip as it propagates. However, the signal is dominated by the arrival of a large-amplitude, coherent wavefront just after the diffuse *P*-wave arrival. The relative amplitude of this wavefront, when compared to the first *P*-wave amplitude, increases with distance to the fault. This is expected because the geometric attenuation of a conic wavefront is smaller than that of spherical one. At each station, the arrival time of this wavefront is consistent with the predicted arrival time of the Mach wavefront.

To confirm our estimations of the rupture velocity, we used two-dimensional (2D) steady-state rupture model to conduct simulations (*21*). We observe an excellent fit, both in relative amplitude and for the general waveform shape, when comparing the experimental waveforms recorded on the MFA sensors during a subshear event and the synthetics obtained by our numerical simulation (Fig. 3B). We observed similar good correspondence between experimental waveforms and simulation of a supershear rupture (Fig. 3C). In both cases, we obtained the best fit between analytical and experimental records by using the rupture velocity estimated experimentally, confirming that our experimental estimate of the rupture velocity is accurate. Furthermore, we show that dynamic rupture models that can accurately simulate strong ground motions on the kilometric scale can also simulate accelerations in the kilohertz range on centimetric sized samples. In other words, dynamic rupture propagation is truly a self-similar mechanism.

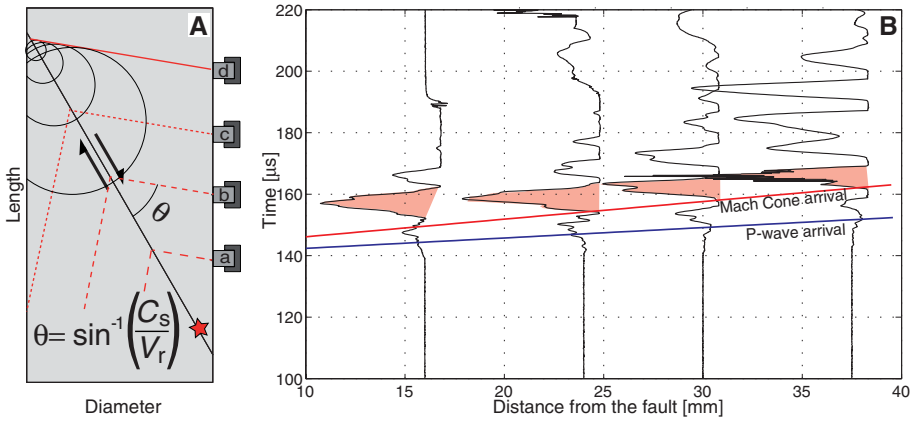

Fig. 2. Mach wavefront arrival. (**A**) Schematic of the Mach cone arrival at MFA stations. The red star represents the nucleation zone of the event. Arrows indicate the sense of shear (here, right lateral). The positions of the MFA stations a to d are shown relative to the fault plane. θ, is the angle of the Mach cone, a function of the ratio between the rupture and shear wave velocities. (**B**) Waveforms recorded on the MFA array during a supershear event that occurred at $\tau = 84$ and $\sigma_n = 99$ MPa. Blue and red solid lines represent the first *P*-wave front and the *S*-wave Mach front, respectively. The Mach front is shaded in red.

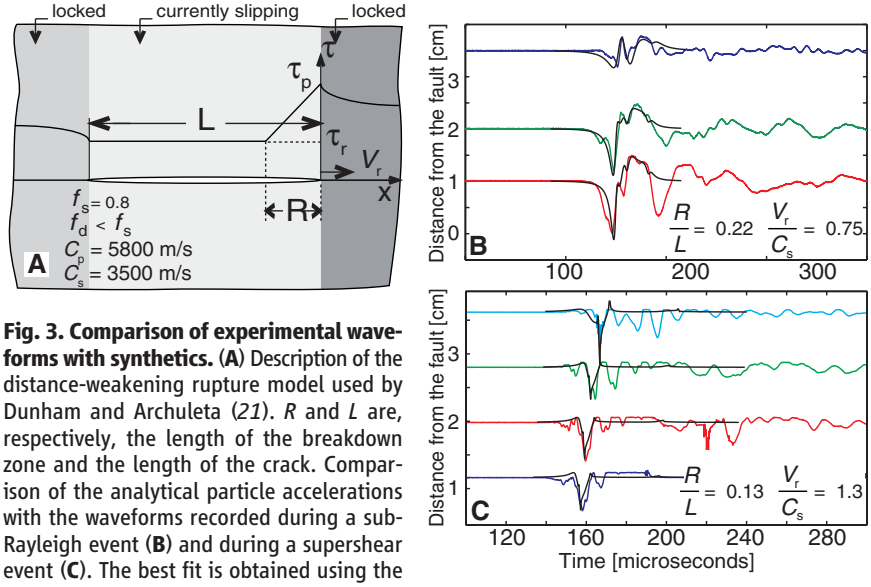

Fig. 3. Comparison of experimental waveforms with synthetics. (**A**) Description of the distance-weakening rupture model used by Dunham and Archuleta (*21*). *R* and *L* are, respectively, the length of the breakdown zone and the length of the crack. Comparison of the analytical particle accelerations with the waveforms recorded during a sub-Rayleigh event (**B**) and during a supershear event (**C**). The best fit is obtained using the inverted rupture velocity.

To confirm our estimations of the rupture velocity, we used two-dimensional (2D) steady-state rupture model to conduct simulations (*21*). We observe an excellent fit, both in relative amplitude and for the general waveform shape, when comparing the experimental waveforms recorded on the MFA sensors during a subshear event and the synthetics obtained by our numerical simulation (Fig. 3B). We observed similar good correspondence between experimental waveforms and simulation of a supershear rupture (Fig. 3C). In both cases, we obtained the best fit between analytical and experimental records by using the rupture velocity estimated experimentally, confirming that our experimental estimate of the rupture velocity is accurate. Furthermore, we show that dynamic rupture models that can accurately simulate strong ground motions on the kilometric scale can also simulate accelerations in the kilohertz range on centimetric sized samples. In other words, dynamic rupture propagation is truly a self-similar mechanism.

Our experimental results demonstrate that the ruptures were dominantly mode II (fig. S3). For this mode, the transition between sub-Rayleigh and supershear rupture has been extensively discussed in theoretical and experimental studies (*9*, *12*–*15*). Following 2D numerical studies, this transition is generally explained in terms of the seismic ratio $S = (\tau_p - \tau_o)/(\tau_o - \tau_r)$ where τ_p, τ_o, and τ_r are the peak frictional strength, the initial shear stress, and the residual frictional strength, respectively. The ratio τ_o/σ_n (where σ_n is the normal stress), employed by Ben-David *et al.* (*14*), is equivalent to *S*, and both quantities are simply related by $\tau_o/\sigma_n = (f_s - f_d)/(1 + S) + f_d$ (where f_s and f_d are the static and dynamic friction coefficients, respectively) (Fig. 4). In our experiments, τ_o was continuously measured (Fig. 1). Taking $f_s = 0.85$ and $f_d = 0.1$, *S* could be estimated for each individual stick-slip. Supershear propagation may happen under both of the following conditions: (i) $S < S_c$ (where S_c, the critical value of *S* allowing supershear transition, is equal to 1.77 or 1.119 in 2D and 3D, respectively), which was always the case in our experiments (Fig. 4A), and (ii) when the rupture length exceeds the transition length *L*, estimated following the semi-empirical relation (*9*)

$$L = \frac{39.2}{\pi(1-\upsilon)} \frac{1}{(S_c - S)^3} \frac{\mu G}{\left[\sigma_n \left(\frac{f_s - f_d}{1+S}\right)\right]^2} \quad (1)$$

where υ, μ, and *G* are, respectively, the Poisson ratio, the shear modulus, and the fracture energy. In our case, condition (ii) can be met only if $L < L_f$, where L_f is the finite length of the experimental fault. In our experiments, *G* may range from

the lower bound 10 J/m^2, as given by single-crystal fracture energy values and stick-slip experiments performed at low normal stress (*19*), to the upper bound 10^4 J/m^2, measured for intact Westerly granite samples at high confining pressures (*22*). From Eq. 1, L was calculated as a function of normal stress in two cases: (i) $S = 1$ and $G = 10$ J/m^2 and (ii) $S = 0$ and $G = 1000$ J/m^2 (Fig. 4A). Experiments performed at the lowest normal stresses are compatible with $G \approx 10$ J/m^2. However, experiments performed at intermediate normal stresses can be explained only by using larger fracture energy. This is consistent with our observation of an intense production of fine gouge particles at intermediate and high normal stresses. Indeed, for spherical particles, the ratio between G and surface energy of single crystals (γ) is $G/\gamma \approx 3w/d$, where w is the fault thickness and d is the average particle size. Our observation of gouge particles of 1-μm diameter and smaller is consistent with a fault roughness of less than 30 μm. The match between the measured rupture velocities and the prediction that the minimum transition length L drops to a few centimeters (comparable to our sample size) at high normal stress (Fig. 4A) explains why, in our experiments, supershear rupture becomes a "normal" phenomena for $\sigma_n >$ 60 MPa. It also explains why supershear ruptures were not clearly observed in previous experimental studies on rocks conducted at low normal stress (most often in biaxial conditions) (*18*, *19*).

Finally, we observe a double correlation between the rupture velocity, the initial stress ratio τ_o/σ_n, and the final stress drop (Fig. 4B). Subshear ruptures occurred for stress ratios $\tau_o/\sigma_n <$ 0.6 and resulted in stress drops generally lower than 1.5 MPa. Conversely, supershear ruptures occurred for stress ratios $\tau_o/\sigma_n > 0.7$ and resulted in stress drops generally larger than 3 MPa. These results not only make sense physically but are also compatible with values previously observed on brittle polymers (*14*) and with field observations for the Kunlunshan earthquake (*23*). Importantly, our findings are comparable to the average stress drops inferred by seismologists for most large crustal earthquakes. Note that our direct measurement of the stress drop is comparable to what a seismological estimate would be using the final slip u (fig. S4).

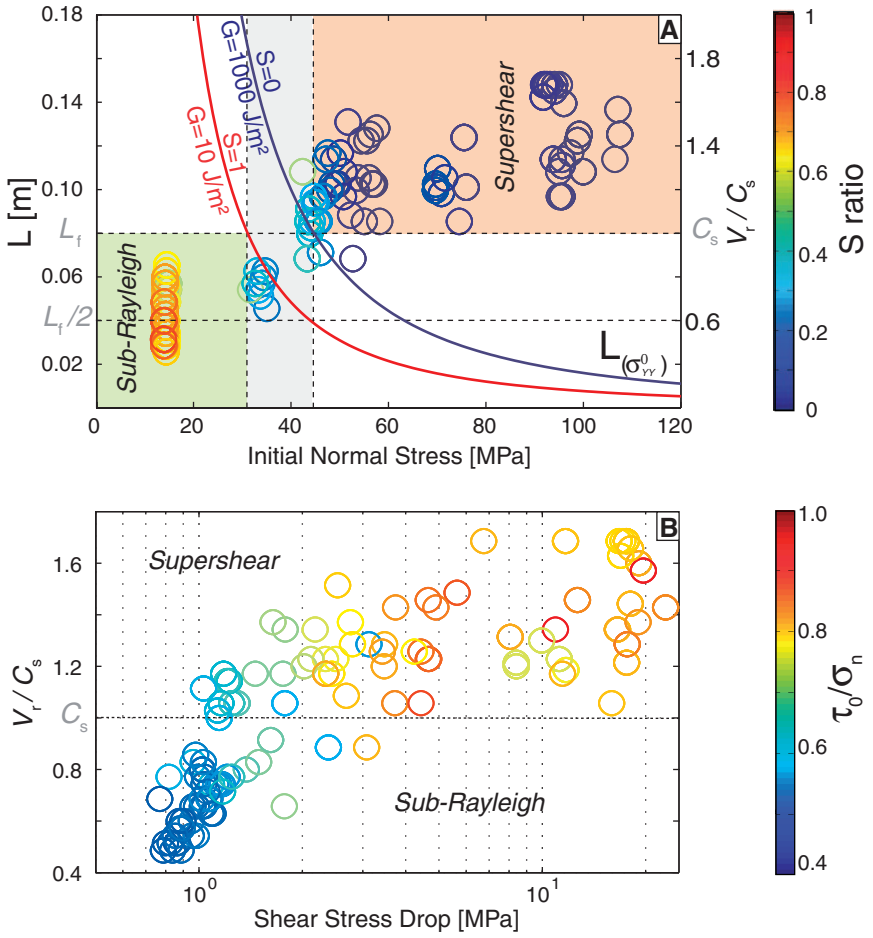

Fig. 4. The transition to supershear ruptures. (**A**) Correlation between normal stress and rupture velocity. Color-coding corresponds to the value of S. Red and blue solid lines represent L as a function of normal stress, assuming two combinations of S and G. (**B**) Correlation between rupture velocity and stress drop. Color-coding corresponds to the value of τ_o/σ_n. L_f is the length of the experimental fault and $L_{(\sigma^0_{YY})}$ is the transition length as a function of the normal stress.

Based on our experimental results, why is there a paucity of supershear ruptures observed in nature? A first straightforward explanation is related to the difference in fault geometry between our experiments and seismogenic faults. Our experiments consisted of a perfectly planar fault geometry with very low initial roughness at high normal stress, leading to uniform and large stresses on the fault plane. Seismogenic faults, on the other hand, are most often nonplanar and exhibit self-affine roughness (*24*). The occurrence of kinks and dilatational jogs could slow down or even arrest locally the propagation of seismic ruptures (*25*). The few documented examples of supershear earthquakes are on very smooth, planar fault sections (*3*–*8*). In addition, the presence of a gouge layer along the fault interface may slow the propagation of the rupture, as well as thermo-hydro-mechanical coseismic processes within the breakdown zone [such as thermal pressurization (*26*), frictional melting (*27*), mineral reactions (*28*), and off fault damage, including pulverization (*29*)], which dissipate part of the released strain energy available, resulting in a deceleration of the rupture front. Alternatively, the paucity of supershear rupture observation in nature might also be due to limitations in instrumentation and/or spatial coverage. Nevertheless, the experimental values of L and stress drops reported here for a classical crustal lithology (Westerly granite) under upper-crustal conditions (<150 MPa) demonstrate that rupture velocity may exhibit important variations at the scale of small (centimetric) asperities, so that the seismological estimate of rupture velocities over long fault segments is an average that could well have little importance at the scale of an asperity. Our experimental results strongly suggest that, despite the scarcity of compelling measurements on natural earthquakes, supershear ruptures may frequently occur at the local scale of asperities, for which the stress drop generally inferred is quite large. In turn, these sudden accelerations and decelerations of the rupture front should play an important role in generating high-frequency radiation, which will influence the total rupture-energy budget.

References and Notes

1. R. Madariaga, *Ann. Geophys.* **1**, 17 (1983).
2. R. Burridge, *Geophys. J. R. Astron. Soc.* **35**, 439 (1973).
3. R. J. Archuleta, *J. Geophys. Res.* **89**, 4559 (1984).
4. M. Bouchon *et al.*, *Geophys. Res. Lett.* **28**, 2723 (2001).
5. M. Bouchon, M. Vallée, *Science* **301**, 824 (2003).
6. W. L. Ellsworth *et al.*, *Earthq. Spectra* **20**, 597 (2004).
7. P. Liu, S. Custdio, R. J. Archuleta, *Bull. Seismol. Soc. Am.* **96**, S143 (2006).
8. D. Wang, J. Mori, T. Uchide, *Geophys. Res. Lett.* **39**, L21307 (2012).
9. D. J. Andrews, *J. Geophys. Res.* **81**, 5679 (1976).
10. A. Bizzarri, E. M. Dunham, P. Spudich, *J. Geophys. Res.* **115**, B08301 (2010).
11. F. T. Wu, K. C. Thomson, H. Kuenzler, *Bull. Seismol. Soc. Am.* **62**, 1621 (1972).
12. K. Xia, A. J. Rosakis, H. Kanamori, *Science* **303**, 1859 (2004).
13. S. Nielsen, J. Taddeucci, S. Vinciguerra, *Geophys. J. Int.* **180**, 697 (2010).
14. O. Ben-David, G. Cohen, J. Fineberg, *Science* **330**, 211 (2010).

15. A. Schubnel, S. Nielsen, J. Taddeucci, S. Vinciguerra, S. Rao, *Earth Planet. Sci. Lett.* **308**, 424 (2011).
16. W. F. Brace, J. D. Byerlee, *Science* **153**, 990 (1966).
17. T. L. Johnson, C. H. Scholz, *J. Geophys. Res.* **81**, 881 (1976).
18. P. G. Okubo, J. H. Dieterich, *J. Geophys. Res.* **89**, 5817 (1984).
19. M. Ohnaka, L.-f. Shen, *J. Geophys. Res.* **104**, 817 (1999).
20. M. Mello, H. S. Bhat, A. J. Rosakis, H. Kanamori, *Tectonophysics* **493**, 297 (2010).
21. E. M. Dunham, R. J. Archuleta, *Geophys. Res. Lett.* **32**, L03302 (2005).
22. T.-F. Wong, *J. Geophys. Res.* **87**, 990 (1982).
23. D. P. Robinson, C. Brough, S. Das, *J. Geophys. Res.* **111**, B08303 (2006).
24. T. Candela, F. Renard, *J. Struct. Geol.* **45**, 87 (2012).
25. R. H. Sibson, *Nature* **316**, 248 (1985).
26. J. R. Rice, *J. Geophys. Res.* **111**, B05311 (2006).
27. G. Di Toro, T. Hirose, S. Nielsen, G. Pennacchioni, T. Shimamoto, *Science* **311**, 647 (2006).
28. N. Brantut, A. Schubnel, J.-N. Rouzaud, F. Brunet, T. Shimamoto, *J. Geophys. Res.* **113**, B10401 (2008).
29. M.-L. Doan, G. Gary, *Nat. Geosci.* **2**, 709 (2009).

Acknowledgments: We thank Y. Pinquier for technical support and two reviewers and the associate editor for their constructive remarks, which helped to enhance this paper. F.X.P., A.S., and S.N. acknowledge support from the French and Italian Ministry of Foreign affairs program GALILEO, project no. 26019WJ. This work was supported by the Institut National des Sciences de l'Univers. Data are available in the supplementary materials.

Supplementary Materials
www.sciencemag.org/cgi/content/full/340/6137/1208/DC1
Materials and Methods
Figs. S1 to S4
Table S1
References

25 January 2013; accepted 15 April 2013
10.1126/science.1235637

Stepwise Evolution of Essential Centromere Function in a *Drosophila* Neogene

Benjamin D. Ross,[1,2] Leah Rosin,[3]* Andreas W. Thomae,[4]* Mary Alice Hiatt,[2,5]* Danielle Vermaak,[2]*† Aida Flor A. de la Cruz,[2,6] Axel Imhof,[4] Barbara G. Mellone,[3] Harmit S. Malik[2,6]‡

Evolutionarily young genes that serve essential functions represent a paradox; they must perform a function that either was not required until after their birth or was redundant with another gene. How young genes rapidly acquire essential function is largely unknown. We traced the evolutionary steps by which the *Drosophila* gene *Umbrea* acquired an essential role in chromosome segregation in *D. melanogaster* since the gene's origin less than 15 million years ago. Umbrea neofunctionalization occurred via loss of an ancestral heterochromatin-localizing domain, followed by alterations that rewired its protein interaction network and led to species-specific centromere localization. Our evolutionary cell biology approach provides temporal and mechanistic detail about how young genes gain essential function. Such innovations may constantly alter the repertoire of centromeric proteins in eukaryotes.

Young essential genes (*1*) challenge long-standing dogmas about the relationship between essentiality and conservation (*2*). Partitioning of essential, ancestral functions (subfunctionalization) between (old) parental and (young) daughter genes (*3*, *4*) explains one route by which young genes become essential. More difficult to understand is how new genes become essential via the emergence of novel function (neofunctionalization) (*5*). This could result from partial duplication of ancestral genes, novel gene fusions, or rapid amino acid changes (*6*). The contribution of each of these processes to the acquisition of essential function is unknown, as are the underlying molecular changes.

To gain insight into the birth and evolution of essential function, we focused on one newly evolved gene in *Drosophila*. *Umbrea* (also known as *HP6* and *CG15636*) arose via duplication of the intronless *Heterochromatin Protein 1B* (*HP1B*) gene into an intron of the *dumpy* gene (Fig. 1A) (*7*). HP1B is a chromosomal protein that predominantly localizes to heterochromatin in *D. melanogaster* cells and regulates gene expression (*8*). *HP1B* is dispensable for viability (*8*), yet RNA interference (RNAi) knockdown phenotypes show *Umbrea* to be essential in *D. melanogaster* (*1*, *9*). The 100% late larval-pupal lethality upon *Umbrea* knockdown could be rescued by an Umbrea–green fluorescent protein (GFP) fusion (fig. S1). Genetic knockout experiments (fig. S1) further confirmed that *Umbrea* is essential in *D. melanogaster*.

We traced *Umbrea*'s evolutionary path after duplication from *HP1B* to understand when and how essential function was gained by comparing the localization of HP1B and Umbrea proteins in *D. melanogaster* Kc cells. GFP-tagged HP1B proteins from both *D. melanogaster* and *D. ananassae* [whose divergence predates the birth of *Umbrea* (*7*)] localized to pericentric heterochromatin and euchromatin (Fig. 1B and fig. S2). In contrast, Umbrea-GFP predominantly localized to interphase centromeres, but not telomeres (Fig. 1C and fig. S3, A and B). Specific antibodies raised against Umbrea (fig. S4A) confirmed its centromere localization in developing spermatocytes and larval imaginal discs (Fig. 1, D and E, and fig. S4, B and C).

On the basis of its essentiality and centromere localization, we hypothesized that Umbrea was required for chromosome segregation. Upon depletion of Umbrea by RNAi knockdown (fig. S5A), relative to control cells, *D. melanogaster* S2 cells displayed increased mitotic errors, including delayed chromosome alignment, early anaphase onset, lagging anaphase chromosomes, and multipolar configurations ($P < 0.05$) (Fig. 1, F and G, fig. S5B, and movies S1 to S3). These data suggest that Umbrea promotes proper chromosome segregation, but is not required for the localization of the centromeric histone Cid (Fig. 1F).

To date the origin of *Umbrea* and subsequent changes, we sequenced the *Umbrea* locus from 32 *Drosophila* species (fig. S6A). Whereas *HP1B* was preserved (*7*), we found *Umbrea* in only 20 of 32 species, dating its monophyletic origin to 12 to 15 million years ago (Fig. 2A and fig. S6B). Using maximum likelihood methods, we observed evidence of both episodic and recurrent positive selection acting on *Umbrea* (fig. S7, A to D). These findings, together with the altered localization, lead us to conclude that neofunctionalization, not subfunctionalization, drove the divergence of *Umbrea* (*10*). Although *Umbrea* is essential in *D. melanogaster*, it was lost at least three independent times—in *D. fuyamai*, *D. eugracilis*, and in the suzukii clade (Fig. 2A)—which suggests that *Umbrea* was not essential at or immediately after its birth.

Four lineages retained full-length *Umbrea* genes, two of which encode an intact chromodomain (CD) and ancestral residues essential for binding histone H3 trimethyl Lys^9 (H3K9me) (fig. S8) (*11*). However, most extant *Umbrea* genes have lost their CDs, and encode only the chromoshadow domain (CSD), which mediates protein-protein interactions (*12*) (Fig. 2A). We first tested how CD loss affected HP1B function. We found that an HP1B-GFP fusion lacking the CD lost heterochromatin localization (Fig. 2B), consistent with the requirement of HP1 CD for H3K9me binding (*13*). Furthermore, fusion of the HP1B CD and hinge to Umbrea-GFP reverted localization from centromeres to heterochromatin (Fig. 2C), which suggests that loss of the ancestral CD

[1]Molecular and Cellular Biology Program, University of Washington, Seattle, WA 98195, USA. [2]Basic Sciences Division, Fred Hutchinson Cancer Research Center, Seattle, WA 98109, USA. [3]Department of Molecular and Cell Biology, University of Connecticut, Storrs, CT 06269, USA. [4]Munich Centre of Integrated Protein Science and Adolf-Butenandt Institute, Ludwig Maximilians University of Munich, 08336 Munich, Germany. [5]Law Firm of Fitzpatrick, Cella, Harper & Scinto, New York, NY 10104, USA. [6]Howard Hughes Medical Institute, Fred Hutchinson Cancer Research Center, Seattle, WA 98109, USA.

*These authors contributed equally to this work.
†Present address: Science-wise Consulting, Seattle, WA 98109, USA.
‡Corresponding author. E-mail: hsmalik@fhcrc.org

www.sciencemag.org/cgi/content/full/340/6137/1208/DC1

Supplementary Materials for

From Sub-Rayleigh to Supershear Ruptures During Stick-Slip Experiments on Crustal Rocks

François X. Passelègue,* Alexandre Schubnel, Stefan Nielsen, Harsha S. Bhat, Raùl Madariaga

*Corresponding author. E-mail: passelegue@geologie.ens.fr

Published 7 June 2012, *Science* **340**, 1208 (2012)
DOI: 10.1126/science.1235637

This PDF file includes:

Other Supplementary Material for this manuscript includes the following:
(available at www.sciencemag.org/cgi/content/full/340/6137/1208/DC1)

Materials and Methods

Experimental Set-up

The apparatus used here is a tri-axial oil medium loading cell ($\sigma_1 > \sigma_2 = \sigma_3$) built by Sanchez Technologies (Fig. S1A). The apparatus can support a confining pressure of 100 MPa and up to 600 MPa in differential stress (for 40 mm sample diameter). The confining pressure ($\sigma_2 = \sigma_3$) and the axial stress (σ_1) are servo-controlled independently. Experiments are conducted by imposing a constant strain rate, ranging from 10^{-5}/s to 10^{-4}/s. Displacement is measured externally by three gap sensors and then corrected from the machine stiffness. Stresses and strains are monitored at 10 Hz sampling rate.The piezo-ceramic sensors used consist of a PZT crystal (PI ceramic PI255, 5 mm in diameter and 0.5 mm in thickness) encapsulated within a brass casing. All the piezoelectric crystals are polarised in the same way and record preferentially compressional waves. The signal received on each sensor is unamplified and relayed to a 16 channel digital oscilloscope, at a sampling rate of 10 MHz. The waveforms recorded correspond to the variation of the particles acceleration during instability. More information about the apparatus and the acoustic system can be found in (*S1*,*S2*).

Sample preparation

The rock used in this study was Westerly Granite Blue (*S3*). *P* and *S* wave velocities were measured in the sample and are respectively C_p = 5800 m/s and C_s = 3500 m/s. The Rayleigh wave velocity (C_R) was estimated at 3200 m/s. A rock sample consists in a cylinder of granite with a diameter of 40 mm and a length of 88 mm. Both basal areas are rectified with a surface grinder. The cylinder is then cut at an angle of 30° with the vertical to simulate a natural fault interface. The fault surface of each half-sample is first grinded to assure a perfect contact. A small roughness is then applied using #240 grit papers to preserve an efficient cohesion during the first step of the experiments.

Acoustic sensors were placed at various positions with respect to the fault, as described in Figs. S1B and S1C. The position of each is measured with an accuracy of ±1mm. The sealing between the sample and the sensors is provided by two layers of flexible and non brittle adhesive. The sample is isolated from the confining oil using a viton jacket (5mm wall thickness).

Rupture velocity inversion method

Photoelastic dynamic rupture experiment coupled with acoustic high frequency recording has highlighted the fact that piezoceramic sensors located close to the fault plane record the passage of the rupture front, corresponding to the first wave arrival observed in the travel time plot (*15*). Transducers located actually record the passage of the rupture front, because in the near-field, the elastic strain is dominated by the r^{-n} (n = ½ in sub-Rayleigh; $0 < n \leq ½$ in supershear) singularity close to the rupture tip.

For each stick-slip event, the first wave arrival recorded on each sensor during each event was manually picked for a better accuracy (the accuracy of picking is in the order of 0.1μs). To estimate the average rupture velocity, the first step consists in the calculation of the theoretical travel times between a nucleation point (X,Y) on the fault plane and the near-field piezoelectric sensor array locations (X_k,Y_k). Because of the 3D experimental geometry, a complex mixed-mode rupture can develop. As a consequence, rupture propagates in mode II (in plane) along the fault length, while in mode III (antiplane) along the fault width (Fig. S2A). The theoretical travel times can be calculated by the expression:

$$t_{(i,k)} = \frac{\sqrt{(X - Xk) + (Y - Yk)}}{\sqrt{C_{III}^2 \cos\theta + C_{II}^2 \sin\theta}} \qquad (1)$$

where θ is the angle between rupture front propagation direction and the in-plane direction, C_{II} and C_{III} being respectively the in-plane and the antiplane rupture velocity (Fig. S2A). If $C_{II}<C_s$ (with C_s the shear wave velocity), we impose a circular rupture front and $C_{II}=C_{III}$. Conversely, If $C_{II}>C_s$, we impose an elliptic rupture front with $C_{III}=C_s$ and $C_{II}>C_s$.

Time residuals are calculated between experimental arrival times ($t^{\exp}$) and the theoretical ones for different rupture initiation times (t^0) following:

$$\Delta t(C_{II}, k, to) = \sqrt{\frac{\sum_i^n \left| t_{(i,k)}^{\exp} - t_{(i,k)} - t_i^0 \right|}{n}} \qquad (2)$$

The sum of the residual time for each sensor is then computed for one nucleation point, one initiation time and one rupture velocity using a least-square function and then computed for each location *(X,Y)* of the fault plane, for all possible rupture velocities (*S4*) and for different initiation times. A simple least square minimisation outputs the nucleation point of the event, its time of initiation and the in-plane rupture velocity. Figs. S2B and S2C display the lowest value of σ for all C_{II} inverted for a sub Rayleigh and a supershear event respectively.

Figs. S2D and S2E are travel-time plots of the rupture history, which display the waveforms recorded by near field sensors as a function of the distance from the nucleation zone for events #31 (sub-Rayleigh) and #41 (supershear). Both of these recordings were obtained during an experiment at 30 MPa confining pressure. The signals are normalized by the maximum amplitude of each trace. In the case of SSE #31 (Fig. 1D), the alignment of the first arrivals shows an average rupture velocity V_r of 3100 m/s, i.e. close to the Rayleigh wave speed (C_R = 3200 m/s). On the contrary, in the case of SSE #41 (Fig. 1E), the inversion shows a rupture faster than the shear waves peed (C_s = 3500 m/s), with an average velocity of 5300 m/s.

Analytical modeling

The 2D model (*21*) assumes a linear breakdown zone, with distance, between the peak and the residual frictional strengths (Fig. 3A). The ratio between the dimension of the breakdown zone (R) and the crack length, R/L, is adjusted to fit the experimental waveforms (≈ 0,175 ± 0,045 in all our simulations). The initial frictional peak strength and rupture velocity used in the simulation are that directly measured during the experiment. All the parameters used in the simulation are given in Fig. 3. Because of the lack of calibrated accelerometers, the residual friction coefficient (f_d) is adjusted to fit the maximum amplitude of a single waveform recorded away from the fault. The strength drop, $(f_s - f_d)(-\sigma^0_{yy})$, is related to the particle velocity at any location (x, y), in steady-state rupture models, as:

$$\mathring{u}\left(\frac{x}{L},\frac{y}{L}\right)=\frac{(f_s-f_d)(-\sigma^0_{yy})}{\mu}\Omega\left(\frac{x}{L},\frac{y}{L},\frac{R}{L},\frac{V_r}{C_s}\right) \tag{3}$$

where $\mathring{u}$ is the particle velocity, μ is the shear modulus, f_s is the static friction and σ^0_{yy} is the total normal stress. The precise expression of the complex analytic function Ω can be found in (*20*). When the amplitude is fitted for one waveform (by adjusting R/L and f_d), only the distance to the fault plane is changed to simulate the remaining far-field waveforms. Thus the focus here is only the relative amplitude with respect to distance from the fault. Unfortunately, the absolute value of acceleration cannot be discussed because of the lack of sensor calibration.

The geometry of the fault in our experiment is expected to impose a complex mixed mode rupture front as described above. However, the numerical simulations of the particles acceleration using a 2D model (*21*) present an excellent fit with the experimental waveforms recorded on far-field sensors. These results suggest that the rupture is dominantly Mode II in our experiments. The explanation is given by the fact that events mostly nucleate at one of the fault tips (*S5*), inducing a dominant mode II front when the rupture arrives on far-field sensors (Fig. S3).

Estimation of the transition length

To estimate the transition length to supershear (L) in our loading conditions, we can start with the definition of the critical nucleation length (L_c) adapted from Andrews 1976 (*9*):

$$L_c=\frac{4}{\pi}\frac{\mu}{1-\nu}\frac{G}{(\tau_0-\tau_r)} \tag{4}$$

where μ is the shear modulus of the rock, ν is the Poisson ratio, G is the fracture energy, τ_0 and τ_r are respectively the initial and the residual shear stresses. The dimensionless stress ratio S is defined by (*9*):

$$S=\frac{\tau_p-\tau_0}{\tau_0-\tau_r} \tag{5}$$

where τ_p is the peak frictional stress. Finally, the transition length L is empirically fit by the polynomial law (*9*):

$$L = 9.8(S_c - S)^{-3} L_c \tag{6}$$

Upon substitution of (4) and (5) into (6) we obtain:

$$L = \frac{4A_1}{\pi(1-\nu)} \frac{\mu G}{(\tau_0 - \tau_r)\left(S_c - \frac{\tau_p - \tau_0}{\tau_0 - \tau_r}\right)^3} \tag{7}$$

where A_1=9.8 and S_c=1.77 or 1.19 in 2D and 3D respectively.

Fracture energy

In our experiments, G should range between 10–1000 J/m^2. The lower bound is given by single crystal fracture energies values and stick slip experiments performed at low normal stress *(19)*, while the upper bound is an order of magnitude smaller than the fracture energies measured for intact Westerly granite samples at high confining pressures *(22)*. Even if G could be close to *10* J/m² at very low normal stresses, the fracture energy increases undoubtedly quickly with the normal stress. This assumption is supported by an intense production of fine gouge particles at the fault interface during our experiments. The total fracture energy corresponds to the product of the crack surface area and the surface energy (γ). Considering particles as spheroids of radius d (average particle size) and a fault zone of thickness w, we can write the simple relation

$$G = NS_a\gamma = \frac{3w}{d}\gamma \tag{8}$$

where N is the number of particles in the fault volume and S_a the average surface of particles. Taking value of γ around 10 J/m² (*19*) and d=1µm, a thickness w in the range of the fault roughness (ω≈30 µm), the value of G is equal to 900 J/m².

Stress drop scaling laws

We present the correlation between the rupture velocity and the final stress drop obtained from direct measurements during our experiments. These measurements are compatible with what seismological estimates would be because of the direct relationship between the final shear stress drop and the displacement u (Fig. S4A). In such a way, we can propose an estimation of the final stress drop using the measure of the displacement by using the formula $\Delta\sigma = C\mu u/L_f$, where μ is the shear modulus, C is a constant of order unity (~1) and L_f the fault length (Fig. S4B). The same correlation is observed and the estimate values are very comparable to our direct measurements.

Supplementary figures:

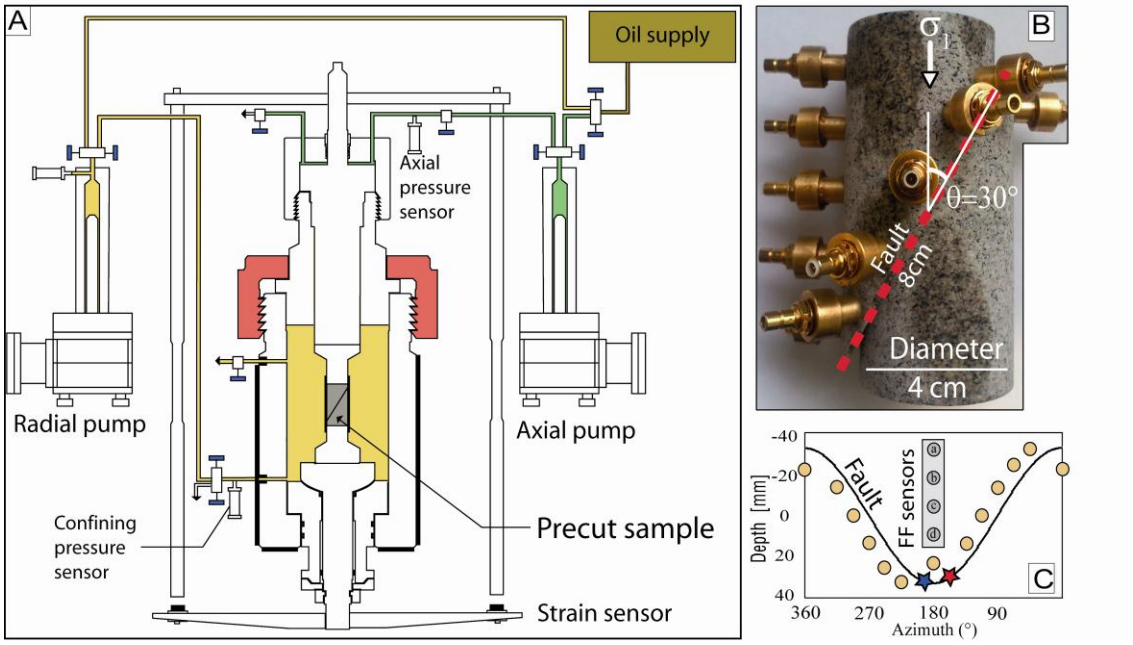

Fig. S1. (A) Schematic of the triaxial apparatus. Axial and radial stresses are driven by two precision microvolumetric high pressure pumps. Axial deformation is measured by the mean of three displacement transducers. (B) The fault system is simulated using a saw cut Westerly granite sample. The fault is inclined at an angle $\mu = 30^{o}$ to σ_1 promoting mixed mode II and III ruptures. (C) Sensor arrays used to estimate the rupture velocity. Gray circles are sensors used to track the Mach cone (MFA). Yellow circles are Near-Field (NF) sensors used to estimate the rupture velocity. Blue and red stars represent respectively the nucleation zones of a sub-Rayleigh event #31 and a supershear event #41 (Fig. S2).

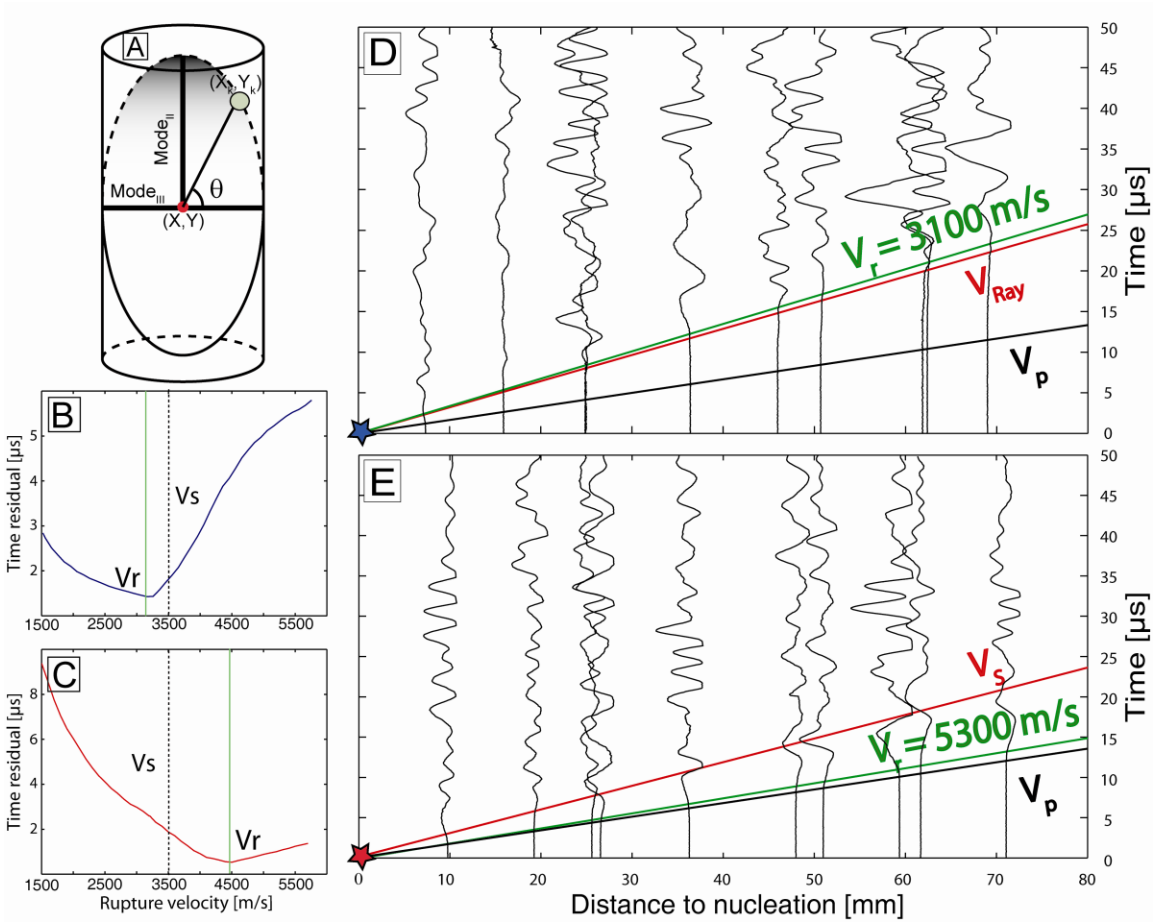

Fig. S2. (A) Mixed mode rupture geometry. (B) Travel time plot of the waveforms recorded on NF sensors, displayed as a function of distance to nucleation during event #31. The alignment of first arrivals (green solid line) indicates the average value of the rupture velocity. Red and black solid lines represent the Rayleigh and the P wave velocities respectively. (C) Time residual as a function of rupture velocity for event #31. The minimum indicates a sub-Rayleigh rupture velocity (circular rupture front). (D) Travel time plot of the waveforms recorded on NF sensors, displayed as a function of the distance to nucleation during event #41. The alignment of the first arrivals (green solid line) indicates the average value of the rupture velocity. Red and black solid lines represent the S and the P wave velocities respectively (Fig. S1C). (E) Time residual as a function of rupture velocity for event #41. The minimum indicates a supershear rupture velocity (elliptical rupture front).

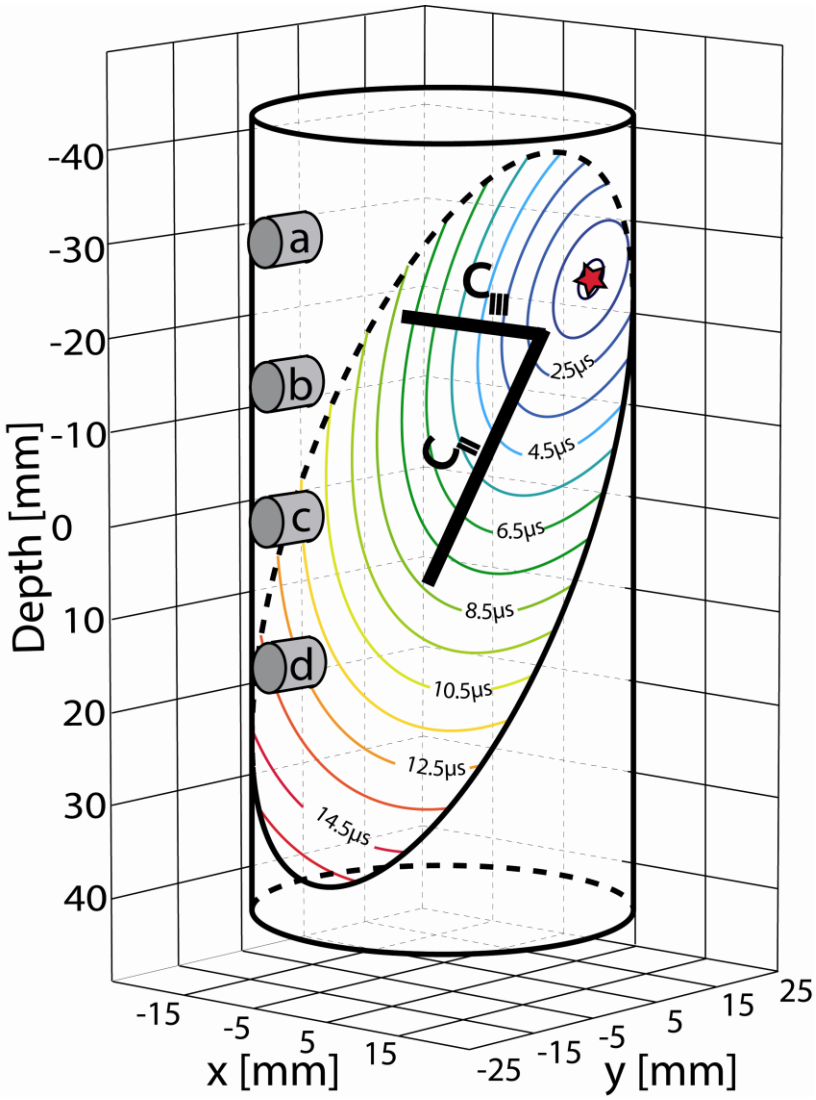

Fig. S3. Propagation of an elliptical (supershear) rupture front at the fault interface during stick slip. The red star represents nucleation point of the event. The rupture front observed on Far-Field sensors (a-d) is dominantly in Mode II.

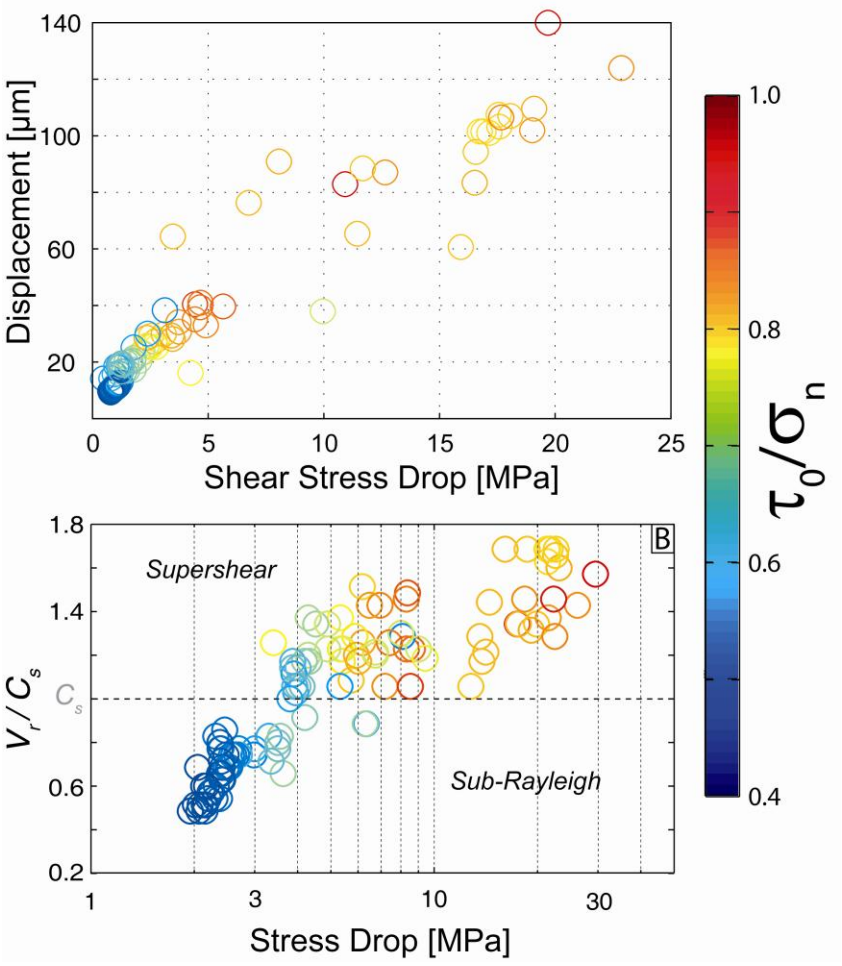

Fig. S4. (A) Correlation between shear stress drop and displacement during stick-slip. (B) Correlation between rupture velocity and "seismological" stress drop, estimated using slip measurements. Color-coding corresponds to the value of τ_o/σ_n.

Supplementary References

S1. N. Brantut, PhD thesis (2011).
S2. N. Brantut, A. Schubnel, Y. Guéguen, *J. Geophys. Res.* **116**, B01404 (2011).
S3. S. S. Goldich, E. H. Oslund, *Geological Society of America Bulletin* **67**, 811 (1956).
S4. S. Das, Tectonophysics **493** (2010).
S5. B. D. Thompson, R. P. Young, D. A. Lockner, *Geophys. Res. Lett.* **32**, L10304 (2005).

References and Notes

1. R. Madariaga, High frequency radiation from dynamic earthquake. *Ann*. *Geophys*. **1**, 17 (1983).

2. R. Burridge, Admissible speeds for plane-strain self-similar shear cracks with friction but lacking cohesion. *Geophys*. *J*. *R*. *Astron*. *Soc*. **35**, 439 (1973). doi:10.1111/j.1365-246X.1973.tb00608.x

3. R. J. Archuleta, A faulting model for the 1979 Imperial Valley earthquake. *J*. *Geophys*. *Res*. **89**, 4559 (1984). doi:10.1029/JB089iB06p04559

4. M. Bouchon *et al*., How fast is rupture during an earthquake? New insights from the 1999 Turkey earthquakes. *Geophys*. *Res*. *Lett*. **28**, 2723 (2001). doi:10.1029/2001GL013112

5. M. Bouchon, M. Vallée, Observation of long supershear rupture during the magnitude 8.1 Kunlunshan earthquake. *Science* **301**, 824 (2003). doi:10.1126/science.1086832

6. W. L. Ellsworth *et al*., Near-field ground motion of the 2002 Denali Fault, Alaska, earthquake recorded at Pump Station 10. *Earthq*. *Spectra* **20**, 597 (2004). doi:10.1193/1.1778172

7. P. Liu, S. Custdio, R. J. Archuleta, Kinematic inversion of the 2004 M 6.0 Parkfield earthquake including an approximation to site effects. *Bull*. *Seismol*. *Soc*. *Am*. **96**, S143 (2006). doi:10.1785/0120050826

8. D. Wang, J. Mori, T. Uchide, Supershear rupture on multiple faults for the M_w 8.6 Off Northern Sumatra, Indonesia earthquake of April 11, 2012. *Geophys*. *Res*. *Lett*. **39**, L21307 (2012).

9. D. J. Andrews, Rupture velocity of plane strain shear cracks. *J*. *Geophys*. *Res*. **81**, 5679 (1976). doi:10.1029/JB081i032p05679

10. A. Bizzarri, E. M. Dunham, P. Spudich, Coherence of Mach fronts during heterogeneous supershear earthquake rupture propagation: Simulations and comparison with observations. *J*. *Geophys*. *Res*. **115**, B08301 (2010). doi:10.1029/2009JB006819

11. F. T. Wu, K. C. Thomson, H. Kuenzler, Stick-slip propagation velocity and seismic source mechanism. *Bull*. *Seismol*. *Soc*. *Am*. **62**, 1621 (1972).

12. K. Xia, A. J. Rosakis, H. Kanamori, Laboratory earthquakes: the sub-Rayleigh-to-supershear rupture transition. *Science* **303**, 1859 (2004). doi:10.1126/science.1094022

13. S. Nielsen, J. Taddeucci, S. Vinciguerra, Experimental observation of stick-slip instability fronts. *Geophys*. *J*. *Int*. **180**, 697 (2010). doi:10.1111/j.1365-246X.2009.04444.x

14. O. Ben-David, G. Cohen, J. Fineberg, The dynamics of the onset of frictional slip. *Science* **330**, 211 (2010). doi:10.1126/science.1194777

15. A. Schubnel, S. Nielsen, J. Taddeucci, S. Vinciguerra, S. Rao, Photo-acoustic study of subshear and supershear ruptures in the laboratory. *Earth Planet*. *Sci*. *Lett*. **308**, 424 (2011). doi:10.1016/j.epsl.2011.06.013

16. W. F. Brace, J. D. Byerlee, Stick-slip as a mechanism for earthquakes. *Science* **153**, 990 (1966). doi:10.1126/science.153.3739.990

17. T. L. Johnson, C. H. Scholz, Dynamic properties of stick-slip friction of rock. *J*. *Geophys*. *Res*. **81**, 881 (1976). doi:10.1029/JB081i005p00881

18. P. G. Okubo, J. H. Dieterich, Effects of physical fault properties on frictional instabilities produced on simulated faults. *J*. *Geophys*. *Res*. **89**, 5817 (1984). doi:10.1029/JB089iB07p05817

19. M. Ohnaka, L.-f. Shen, Scaling of the shear rupture process from nucleation to dynamic propagation: Implications of geometric irregularity of the rupturing surfaces. *J*. *Geophys*. *Res*. **104**, 817 (1999). doi:10.1029/1998JB900007

20. M. Mello, H. S. Bhat, A. J. Rosakis, H. Kanamori, Identifying the unique ground motion signatures of supershear earthquakes: Theory and experiments. *Tectonophysics* **493**, 297 (2010). doi:10.1016/j.tecto.2010.07.003

21. E. M. Dunham, R. J. Archuleta, Near-source ground motion from steady state dynamic rupture pulses. *Geophys*. *Res*. *Lett*. **32**, L03302 (2005). doi:10.1029/2004GL021793

22. T.-F. Wong, Shear fracture energy of Westerly granite from post-failure behavior. *J*. *Geophys*. *Res*. **87**, 990 (1982). doi:10.1029/JB087iB02p00990

23. D. P. Robinson, C. Brough, S. Das, The M_w 7.8, 2001 Kunlunshan earthquake: Extreme rupture speed variability and effect of fault geometry. *J*. *Geophys*. *Res*. **111**, B08303 (2006). doi:10.1029/2005JB004137

24. T. Candela, F. Renard, Segment linkage process at the origin of slip surface roughness: Evidence from the Dixie Valley fault. *J*. *Struct*. *Geol*. **45**, 87 (2012).

25. R. H. Sibson, Stopping of earthquake ruptures at dilational fault jogs. *Nature* **316**, 248 (1985). doi:10.1038/316248a0

26. J. R. Rice, Heating and weakening of faults during earthquake slip. *J*. *Geophys*. *Res*. **111**, B05311 (2006). doi:10.1029/2005JB004006

27. G. Di Toro, T. Hirose, S. Nielsen, G. Pennacchioni, T. Shimamoto, Natural and experimental evidence of melt lubrication of faults during earthquakes. *Science* **311**, 647 (2006). doi:10.1126/science.1121012

28. N. Brantut, A. Schubnel, J.-N. Rouzaud, F. Brunet, T. Shimamoto, High-velocity frictional properties of a clay-bearing fault gouge and implications for earthquake mechanics. *J*. *Geophys*. *Res*. **113**, B10401 (2008). doi:10.1029/2007JB005551

29. M.-L. Doan, G. Gary, Rock pulverization at high strain rate near the San Andreas fault. *Nat*. *Geosci*. **2**, 709 (2009). doi:10.1038/ngeo640

Rupture Velocity [m/s]	Initial axial stress [Mpa]	Confining pressure [Mpa]	Shear stress drop [Mpa]	Displacement [m]
1800	26,61768	10	0,859490307	1,02E-05
2100	26,83501	10	0,875398927	1,01E-05
2100	27,04402	10	0,897948421	1,03E-05
1700	26,87445	10	0,787164604	9,24E-06
1800	27,01304	10	0,798612742	9,56E-06
2400	27,13496	10	0,768646449	9,70E-06
1700	27,2844	10	0,837504333	9,79E-06
1800	27,44369	10	0,824166234	1,01E-05
1800	27,57879	10	0,867344917	9,87E-06
1700	27,74681	10	0,886673674	1,02E-05
2000	27,89372	10	0,877531636	1,05E-05
1900	28,05708	10	0,85213853	1,04E-05
2000	28,25819	10	0,893266865	1,07E-05
2100	28,41319	10	0,949454205	1,10E-05
1900	28,58859	10	0,949350171	1,09E-05
2700	28,7626	10	0,990014685	1,13E-05
1900	28,93647	10	0,982402822	1,12E-05
2900	29,14037	10	1,029829583	1,10E-05
3000	29,29477	10	0,977513197	1,16E-05
2400	29,48823	10	1,069267357	1,19E-05
2400	29,66337	10	1,075838874	1,20E-05
2400	29,85712	10	1,020657202	1,18E-05
2600	30,07432	10	1,119481378	1,22E-05
2600	30,25761	10	1,141298295	1,24E-05
2600	30,46646	10	1,168910805	1,26E-05
2600	30,64758	10	1,163045856	1,26E-05
2700	30,86501	10	1,207754714	1,28E-05
2600	27,96135	10	1,033895601	1,17E-05
2800	27,85996	10	1,020787245	1,13E-05
2700	27,87506	10	1,038048315	1,13E-05
2800	27,91275	10	1,024272403	1,13E-05
2300	27,91613	10	1,036240714	1,13E-05
2300	27,94749	10	0,960126419	1,12E-05
2400	27,93415	10	1,072895563	1,14E-05
2200	27,93221	10	1,085054603	1,14E-05
2300	27,92213	10	1,022755232	1,13E-05

2300	27,9322	10	0,983568876	1,14E-05
2200	27,9411	10	1,099355023	1,15E-05
2500	27,94478	10	1,056137326	1,14E-05
2300	27,95291	10	1,050619159	1,15E-05
2300	27,94761	10	1,096043255	1,22E-05
2200	27,97381	10	1,004843946	1,12E-05
2300	28,00472	10	1,11685017	1,17E-05
2100	28,03498	10	1,12740968	1,17E-05
2100	28,03246	10	1,059501111	1,17E-05
2200	28,06962	10	1,112081919	1,17E-05
2100	28,04253	10	1,124999545	1,16E-05
2200	28,07117	10	1,15540365	1,18E-05
2100	28,10012	10	1,146330968	1,19E-05
2100	28,11454	10	1,155108885	1,19E-05
2100	28,14027	10	1,15222626	1,20E-05
2100	28,17182	10	1,172868454	1,20E-05
2100	28,20144	10	1,157427989	1,20E-05
2000	28,19931	10	1,163106543	1,21E-05
2100	28,2106	10	1,130795138	1,20E-05
2000	28,25466	10	1,19500181	1,22E-05
1900	28,27344	10	1,191651029	1,22E-05
1800	28,29201	10	1,118527728	1,20E-05
1900	28,31553	10	1,210962447	1,24E-05
2000	28,31776	10	1,188512653	1,22E-05
1900	28,35621	10	1,217416926	1,24E-05
2000	28,35917	10	1,066215676	1,20E-05
1900	28,37891	10	1,190177206	1,22E-05
1900	28,35834	10	1,099402705	1,20E-05
1900	28,42406	10	1,214625331	1,23E-05
1800	28,43036	10	1,234539283	1,23E-05
1800	28,41803	10	1,168993166	1,22E-05
1900	28,44741	10	1,123833491	1,21E-05
1800	28,45537	10	1,224478272	1,24E-05
1800	28,52795	10	1,273955382	1,25E-05
1800	28,47221	10	1,241288526	1,25E-05
1800	28,49693	10	1,089298347	1,23E-05
1800	28,53977	10	1,052912255	1,22E-05

1800	28,51885	10	1,176392625	1,23E-05
1800	28,58952	10	1,174515668	1,23E-05
1800	28,60944	10	1,216159841	1,25E-05
1800	28,61095	10	1,247162144	1,25E-05
1700	28,65049	10	1,20487209	1,25E-05
1600	28,69094	10	1,251358206	1,26E-05
1700	28,7022	10	1,131857158	1,23E-05
1800	28,7295	10	1,27016679	1,27E-05
1700	28,78114	10	1,305854983	1,27E-05
1800	28,77572	10	1,167874794	1,25E-05
1800	28,76372	10	1,160176236	1,25E-05
1800	28,78327	10	1,28214377	1,27E-05
1800	28,77688	10	1,237551951	1,27E-05
1800	28,82991	10	1,310445509	1,26E-05
1800	28,86108	10	1,281901023	1,28E-05
1700	28,88237	10	1,207616002	1,26E-05
1700	28,89553	10	1,302716607	1,28E-05
1800	28,90947	10	1,312656244	1,29E-05
1700	28,90685	10	1,332591869	1,29E-05
1800	28,96966	10	1,278281486	1,27E-05
1900	28,99715	10	1,350390451	1,30E-05
1900	28,97705	10	1,247001758	1,28E-05
1900	29,01184	10	1,35078925	1,30E-05
1900	29,02129	10	1,348686885	1,30E-05
1800	29,04253	10	1,254713321	1,29E-05
1700	29,08284	10	1,247699656	1,28E-05
1800	29,06992	10	1,092432389	1,26E-05
1800	29,11569	10	1,238128475	1,29E-05
1800	29,11318	10	1,289070739	1,30E-05
1800	29,15177	10	1,362623183	1,31E-05
1800	29,14735	10	1,34829242	1,32E-05
1800	29,20424	10	1,361669533	1,32E-05
1800	29,17791	10	1,365241386	1,32E-05
1800	29,16204	10	0,915040435	1,26E-05
1900	29,18409	10	1,383365076	1,33E-05
1900	29,22941	10	1,380335069	1,33E-05
1700	29,27548	10	1,400452755	1,34E-05

1800	29,31845	10	1,35760785	1,33E-05
1800	29,32039	10	0,900861389	1,27E-05
1800	29,32657	10	1,387513455	1,34E-05
1800	29,32366	10	1,397804208	1,34E-05
1800	29,35987	10	1,313843972	1,33E-05
1800	29,3411	10	1,285173777	1,32E-05
1900	29,39934	10	1,413985919	1,34E-05
1800	29,39155	10	1,352835263	1,35E-05
1900	29,45585	10	1,010986321	1,30E-05
1800	29,4311	10	1,347460144	1,34E-05
2100	29,4428	10	1,171095531	1,31E-05
1700	29,49844	10	1,353212389	1,34E-05
1800	29,51199	10	1,220282211	1,33E-05
1800	29,50348	10	1,423188644	1,36E-05
1900	29,52572	10	1,389763203	1,36E-05
1700	29,54025	10	1,446249642	1,36E-05
1800	29,54875	10	1,35913369	1,35E-05
4500	86,41674	30	3,126817196	3,83E-05
3100	90,23428	30	2,381679346	3,00E-05
3700	90,73149	30	1,778292354	2,52E-05
3900	91,47551	30	1,03079098	1,85E-05
3500	92,28438	30	1,14535698	1,80E-05
3600	93,28623	30	1,132582693	1,87E-05
3700	94,28731	30	1,158771928	1,86E-05
4100	95,41691	30	1,179718988	1,84E-05
4000	96,17605	30	1,225902946	1,90E-05
4000	97,37918	30	1,208159198	1,83E-05
3700	98,71612	30	1,245408516	1,95E-05
3700	99,92043	30	1,29124617	1,90E-05
3200	101,11751	30	1,617213407	1,99E-05
4100	102,57473	30	1,458389765	1,99E-05
4100	103,87866	30	1,75613756	2,05E-05
4700	105,48151	30	1,782322466	2,14E-05
4800	107,09363	30	1,64215162	2,04E-05
4200	108,73461	30	2,022839207	2,03E-05
4300	110,34888	30	2,116588012	2,32E-05
4700	111,73997	30	2,179481135	2,32E-05

4300	113,72126	30	2,335006233	2,57E-05
4300	115,34713	30	2,503236356	2,53E-05
4800	117,36162	30	2,760964403	2,53E-05
4100	119,86309	30	2,436845563	2,56E-05
4500	120,35203	30	2,799508031	2,78E-05
5300	123,61351	30	2,533421073	2,93E-05
3800	125,73161	30	2,685284006	2,72E-05
3100	127,57622	30	3,078313	2,99E-05
4200	130,28411	30	3,46299607	2,82E-05
4400	131,78028	30	3,419175636	2,93E-05
5000	134,28047	30	3,73736835	3,07E-05
3700	136,94517	30	3,718373579	3,41E-05
5000	139,0381	30	4,897127244	3,30E-05
4400	140,72359	30	4,429274956	3,51E-05
5100	141,72928	30	4,651567452	3,93E-05
4300	143,39777	30	4,670324139	4,10E-05
4300	145,20849	30	4,654311911	3,94E-05
5200	147,17482	30	5,644581002	3,97E-05
3700	149,51568	30	4,43250424	4,04E-05
5500	278,42197	50	19,68973962	0,000139948
4500	250,06238	50	17,66738552	0,000106485
4600	232,78122	50	8,05987926	9,09E-05
5900	226,6427	50	11,68156555	8,85E-05
4700	225,53234	50	16,56782676	9,43E-05
5100	279,93063	50	12,65152323	0,000105688
5100	246,78496	50	2,338281097	8,70E-05
4100	232,65694	50	16,52304421	2,86E-05
4700	232,70589	50	6,750478431	8,34E-05
5900	230,53719	50	11,44585354	7,63E-05
4100	230,52042	50	3,471802807	6,53E-05
4500	230,01841	50	10,92171869	6,44E-05
4700	275,99369	50	17,2945126	8,29E-05
4800	239,69303	50	19,00770629	0,000101927
5000	245,42325	50	22,85932199	0,000123959
5600	234,12152	50	19,0912764	0,000109595
5800	226,35935	50	18,06515305	0,00010702
5900	222,83723	50	17,55904218	0,000107458

5900	220,37786	50	17,58859233	0,000103221
5900	218,48391	50	16,73952716	0,000101489
5700	217,30283	50	16,90046865	0,000101512
5900	217,61099	50	17,15542271	0,000101038
3700	178,68679	40	15,92053786	6,06E-05
5050	182,51947	40	18,03320629	6,87E-05
4150	164,01967	40	11,7194497	4,46E-05
4550	160,92741	40	9,955356403	3,79E-05
4250	159,43454	40	8,395356374	3,20E-05
4200	159,09388	40	8,397882281	3,20E-05
4300	159,27816	40	11,20807987	4,27E-05
4250	184,3577	40	17,60152882	6,71E-05
4400	166,86003	40	4,236577151	1,61E-05
2600	64,75533	20	0,461311816	1,42E-05
2700	68,6202	20	0,81799002	1,42E-05
2900	70,07507	20	0,961306316	1,56E-05
2600	71,55228	20	1,087352872	1,28E-05
2500	72,90999	20	1,171391135	1,59E-05
2700	74,18157	20	1,245225339	1,66E-05
2800	75,45616	20	1,373877095	1,66E-05
2900	76,72626	20	1,492199084	1,69E-05
2300	78,18544	20	1,772368528	1,72E-05
2400	79,29313	20	1,781272154	1,79E-05
2200	80,58932	20	1,749090792	1,81E-05